PNAS RESEARCH ARTICLE | EARTH, ATMOSPHERIC, AND PLANETARY SCIENCES OPEN ACCESS

Increased variability of the western Pacific subtropical high under greenhouse warming

Kai Yang[a], Wenju Cai[b,c,1], Gang Huang[a,d,e,1], Kaiming Hu[a], Benjamin Ng[c], and Guojian Wang[b,c]

Edited by John Wallace, University of Washington, Seattle, WA; received November 11, 2021; accepted April 4, 2022

An anomalous strengthening in western Pacific subtropical high (WPSH) increases moisture transport from the tropics to East Asia, inducing anomalous boreal summer monsoonal rainfall, causing extreme weather events in the densely populated region. Such positive WPSH anomalies can be induced by central Pacific (CP) cold sea-surface temperature (SST) anomalies of an incipient La Niña and warm anomalies in the Indian and/or the tropical Atlantic Ocean, both promoting anticyclonic anomalies over the northwestern Pacific region. How variability of the WPSH, its extremity, and the associated mechanisms might respond to greenhouse warming remains elusive. Using outputs from 32 of the latest climate models, here we show an increase in WPSH variability translating into a 73% increase in frequency of strong WPSH events under a business-as-usual emission scenario, supported by a strong intermodel consensus. Under greenhouse warming, response of tropical atmosphere convection to CP SST anomalies increases, as does the response of the northwestern Pacific anticyclonic circulation. Thus, climate extremes such as floods in the Yangtze River Valley of East China associated with WPSH variability are likely to be more frequent and more severe.

western Pacific subtropical high | East Asia flooding | climate extreme | climate change

Significance

The western Pacific subtropical high (WPSH) channels moisture from the tropics that underpins the East Asian summer climate. Interannual variability of the WPSH dominates climate extremes in the densely populated countries of East Asia. In 2020, an anomalously strong WPSH led to catastrophic floods with hundreds of deaths, 28,000 homes destroyed, and tens of billions in economic damage in China alone. How the frequency of such strong WPSH events will change is of great societal concern. Our finding of an increase in future WPSH variability, translating into an increased frequency of climate extreme as seen in the 2020 episode, highlights the increased risks for the billions of people in the densely populated East Asia with profound socioeconomic consequences.

The western Pacific subtropical high (WPSH) is an anticyclonic system hovering over the middle and lower troposphere of the northwestern Pacific, strongest in boreal summer (1, 2) (*SI Appendix*, Fig. S1*A*). The southerly winds in the west flank of the system transport moisture from the tropics to East Asia and collide with dry and cold flows from the north (2–4). These winds influence *meiyu* (*Baiu* in Japan and *Changma* in Korea) and an associated elongated rain belt that usually starts moving northward from southern China in May before its seasonal southward withdrawal in August, dominating variability of East Asian summer rainfall (3–6). The WPSH undergoes strong interannual variability (*SI Appendix*, Fig. S1*B*), exerting a severe impact on the boreal summer climate over the densely populated region of East Asia (2, 6–8).

A strong WPSH event occurs when the WPSH undergoes a westward intensification, influencing regional climate and leading to anomalous rainfall and inducing severe floods (4, 9). For example, during the 2020 strong WPSH event, floods in the Yangtze River Valley of East China caused hundreds of deaths, millions of hectares of crops destroyed, and tens of billions in economic damage (9, 10). Further back, in 1998, a strong WPSH contributed to river floods in East China that killed thousands and affected more than 200 million people (11).

Previous research examined observed WPSH variability, impact, and change over the period from 1979 to 2017 (12) or response of future climatological WPSH to greenhouse warming in models (13–17). There is an upward trend of the observed WPSH, which is expressed in a leading mode, but whether the WPSH variability above the trend has changed is not clear (12). Other studies found either a stronger or little changed mean WPSH under greenhouse warming (12–17). However, how WPSH variability that rides on the mean state, frequency of strong WPSH anomalies above the mean change, and associated mechanisms will change under future greenhouse warming remain largely unknown.

Multiple processes from ocean basins affect variability of the WPSH (5, 8, 18–22). One process is an atmospheric response to sea-surface temperature (SST) variability in the central Pacific (CP) (Niño4 region, 5°S-5°N, 160°E-150°W), where cool anomalies of an incipient La Niña develop in boreal summer (June, July, and August, JJA) (23); an incipient La Niña suppresses CP local convection, generating a westward propagated atmospheric Rossby wave that strengthens the WPSH (8, 24–29). An enhanced convection over the Maritime Continent associated with the La Niña strengthens the WPSH by modulating local Hadley circulation with increased anticyclonic circulation over the northwestern Pacific (30–32). Anomalous warming of the tropical North Atlantic is also

Author contributions: K.Y. and W.C. designed research; K.Y. performed research; K.H. contributed new reagents/analytic tools; B.N. and G.W. analyzed data; and K.Y., W.C., and G.H. wrote the paper.

The authors declare no competing interest.

This article is a PNAS Direct Submission.

Copyright © 2022 the Author(s). Published by PNAS. This open access article is distributed under Creative Commons Attribution-NonCommercial-NoDerivatives License 4.0 (CC BY-NC-ND).

[1]To whom correspondence may be addressed. Email: Wenju.Cai@csiro.au or hg@mail.iap.ac.cn.

This article contains supporting information online at http://www.pnas.org/lookup/suppl/doi:10.1073/pnas.2120335119/-/DCSupplemental.

Published May 31, 2022.

Downloaded from https://www.pnas.org by CSIRO Library Services on May 31, 2022 from IP address 140.253.235.29.

involved in driving positive WPSH anomalies by inducing CP cold SST anomalies and suppressed convection (33–35).

Another process involves the Indian Ocean, where boreal summer warming induced by a previous-year El Niño triggers warm Kelvin waves emanating into the tropical western Pacific, inducing an anomalous anticyclone at the low troposphere of the northwest Pacific (36, 37). Although the Indian Ocean mechanism can operate by itself with a residual warm condition of the decaying El Niño in the equatorial Pacific, it is in part incorporated in the impact of CP SST variability as the previous-year El Niño transitions to an incipient La Niña.

Because of the vast impact, how variability of the WPSH might change under greenhouse warming is an important issue. Assuming that greenhouse warming has an impact, one expects that observed WPSH variability of the past 42 y (1979 to 2020) should already be impacted. However, due to the short length of observational data and strong internal variability (38), whether change between the latter half (2000 to 2020) and former half (1979 to 1999) period has emerged out of internal variability is not clear. As such, we examine how WPSH variability might change under long-term further increasing greenhouse warming by comparing simulated WPSH variability between two 100-y periods of the 20th and 21st centuries. Over a longer period, impact of greenhouse warming is more detectable because the influence from internal variability is weaker and the climate change signal is larger (39, 40). Below we show that WPSH variability increases under long-term global warming, in turn suggesting that part of the observed change in WPSH variability is driven by greenhouse warming.

Observed WPSH Variability Associated with CP SST

To depict observed WPSH variability we use the circulation field from a reanalysis product (see *Reanalysis Datasets*). We apply an empirical orthogonal function (EOF) analysis (41) to the detrended JJA 850-hPa stream function anomalies referenced to the climatological average of the period 1979 to 2020, in the northwestern Pacific domain (10°N-40°N, 110°E-180°E). We use EOF analysis to identify and separate the main process dominating WPSH variability. The stream function is calculated based on winds (7, 42) and can capture the main characteristics of WPSH variability (30, 34) (see *Indices of WPSH*). We specifically avoid the commonly used geopotential height in the low or middle troposphere (18), as geopotential height is expected to increase with rising tropospheric temperatures under global warming (43–45).

The first two leading EOF patterns and principal component (PC) time series correspond to two components of WPSH variability (Fig. 1 *A* and *B*). EOF1 explains 77% of the total variance and features positive stream function anomalies over the whole northwestern Pacific with maximum anomalies around 20°N, 135°E. Its spatial pattern (Fig. 1*A*) captures main characteristics of a positively abnormal WPSH event, such as coherent high-pressure anomalies over the middle (500 hPa) and low (850 hPa) troposphere, an anomalous anticyclone anomaly at low troposphere, and positive rainfall anomalies in the Yangtze River Valley (*SI Appendix*, Fig. S2).

EOF2 explains 9.3% of the total variance. It is characterized by a southwest–northeast dipole pattern with positive anomalies over the northwest Pacific and negative anomalies to its northeast (Fig. 1*B*) and is associated with anomalous warming in the north Indian Ocean, preceded by a prior-year El Niño event with residual warm anomalies in the Pacific (36, 37) (*SI Appendix*, Fig. S3). Our depiction of WPSH variability above is similar to that in previous studies (8), but the order of the EOFs is different, due in part to the focused domain and data we used (see *Indices of WPSH*).

Time series of our PC1 compares well with other WPSH indices used in previous studies, for example based on areal average of 850-hPa eddy geopotential height over 15°N-25°N, 120°E-150°E (44) or areal average of stream function anomalies over the same domain (30, 34), where highest variability is seen (Fig. 1*C*). Correlation of the PC1 with the areal stream function anomalies average, or the areal eddy geopotential height average, is 0.95 or 0.80, respectively. All the three indices identify four strong positive WPSH events that occurred in 1995, 1998, 2010, and 2020, defined as when an index is larger than a threshold value of 1.5 SD over the 42 y of 1979 to 2020 (Fig. 1*C*) (see *Indices of WPSH*).

EOF2 reflects influence from the Indian Ocean warming, which is in part contributed by a previous-year El Niño, and shows a positive correlation with Niño4 (*SI Appendix*, Fig. S3). Large values of PC1 and PC2 appear in different years. PC2 contributes only to the 1995 and the 2020 strong WPSH events. As such, normalized PC1 is used to assess WPSH variability and identify strong WPSH events.

The PC1 varies coherently with SST variability in the Niño4 region, a positive index being associated with cold Niño4 anomalies, accompanied by anomalous warming over the Maritime Continent/South China Seas and in the tropical Atlantic (Fig. 1*D*; see *Indices of WPSH*). Warm tropical Atlantic anomalies usually peak in JJA and are conducive to an incipient La Niña (33, 46), via anomalous CP easterlies resulting from increased CP subsidence as the tropical Atlantic convection enhances (34, 35). The anomalous CP easterlies contribute to Niño4 cooling and hence to strengthening of the WPSH.

Focusing on the Pacific, the anomalous cooling in the Niño4 region suppresses local convection (*SI Appendix*, Fig. S4), strengthening the WPSH by generating a westward propagated atmospheric Rossby wave (8, 24–27). The positive SST anomalies and enhanced convection over the Maritime Continent associated with La Niña also strengthen the WPSH (*SI Appendix*, Fig. S4) by modulating local Hadley circulation with increased anticyclonic circulation over the northwestern Pacific (30, 31). In addition, easterly anomalies over the equatorial western Pacific associated with the WPSH in turn induce eastward propagating oceanic upwelling Kelvin waves, strengthening the CP cool anomalies, suggesting a positive feedback loop between the CP SST and the WPSH. These processes lead to a correlation coefficient of −0.73 between PC1 and the Niño4 SST, statistically significant above the 99% confidence level (Fig. 1*E*).

Increased WPSH Variability in Future Projection

We use outputs from 32 models participating in the Coupled Model Intercomparison Project phase 6 (CMIP6). These models are forced with historical forcing until 2014 and with Shared Socioeconomic Pathways (SSP) 5–8.5 (SSP5–8.5) emission scenario from 2015 onward to 2099 (47) (see *CMIP Models*). Monthly anomalies are calculated referenced to the climatological mean over the whole period and subsequently quadratically detrended. We apply EOF analysis on JJA stream function anomalies to obtain the WPSH variability pattern and index, as in the observations. Sharing a similar spatial pattern with observation,

Downloaded from https://www.pnas.org by CSIRO Library Services on May 31, 2022 from IP address 140.253.235.29.

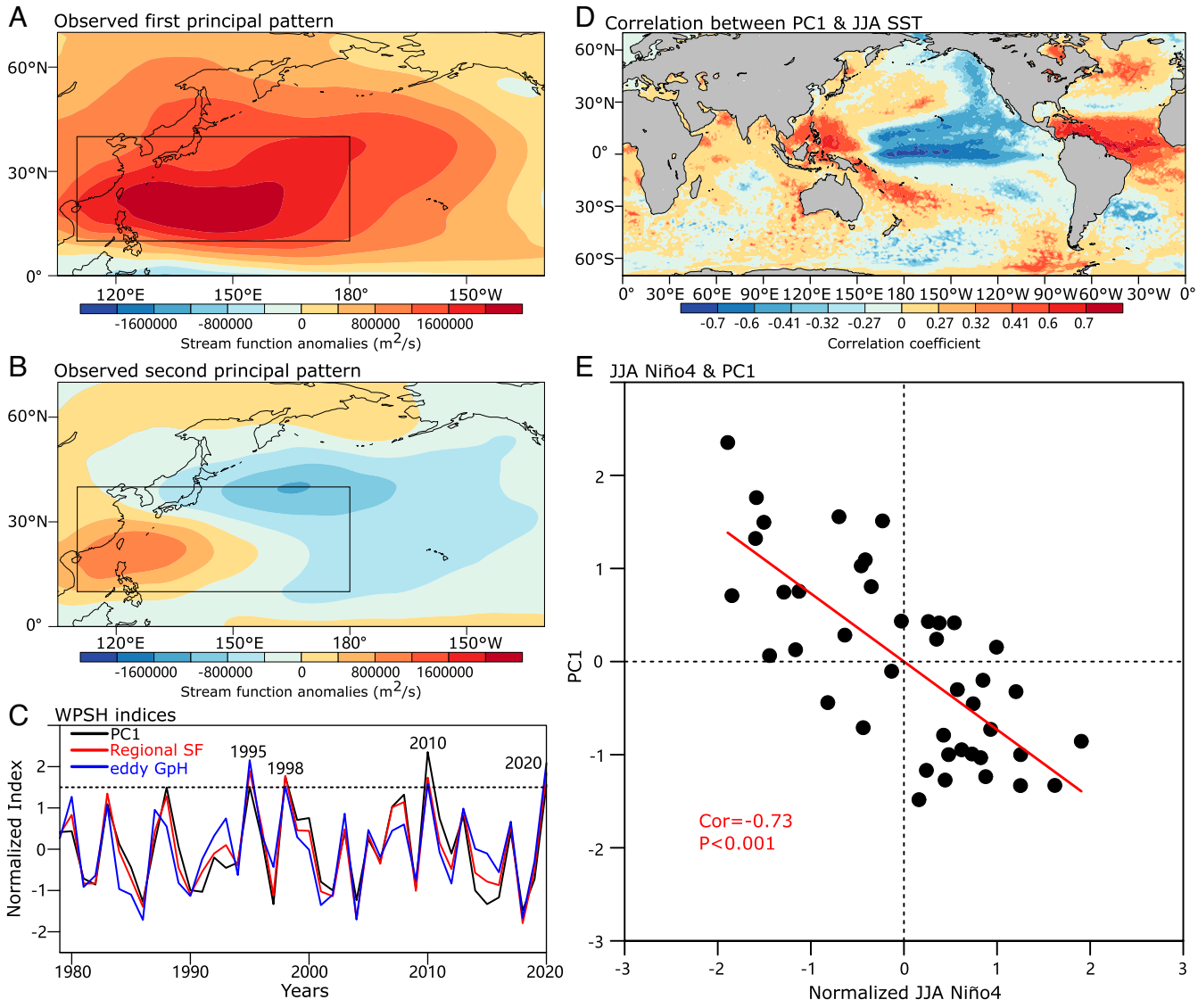

Fig. 1. Depiction of observed WPSH variability. (*A*) JJA averaged 850-hPa stream function anomalies (square meters per second) regressed onto the first PC (PC1) of EOF of JJA 850-hPa stream function anomalies over the northwest Pacific (10°N-40°N, 110°E-180°E) for the period of 1979 to 2020. EOF1 accounts for 77% of the total variance. (*B*) Same as *A*, but for PC2, which accounts for 9.3% of the total variance. The black box in *A* and *B* shows area of our EOF analysis. (*C*) Time series of normalized PC1 (black curve) and regional average of 850-hPa stream function anomalies (Regional SF, red curve) and 850-hPa eddy geopotential height over 15°N-25°N, 120°E-150°E (eddy GpH, blue curve). The black dashed line shows the 1.5 SD value. Years with an index larger than 1.5 SD are identified as 1995, 1998, 2010, and 2020. (*D*) Correlation of JJA SST anomalies with PC1. Correlation coefficients of ±0.27, ±0.32, and ±0.41 are statistically significant above the 90%, 95%, and 99% confidence levels, respectively. (*E*) Relationship between normalized JJA Niño4 and PC1, with a linear fit (red line) and corresponding correlation coefficient (Cor) and *P* value (P) shown. PC1 is principally influenced by Niño4 SST variability. The observed WPSH variability might be influenced by greenhouse warming, but we focus on changes in WPSH variability under future greenhouse warming.

the dominant EOF (EOF1) accounts for 60 to 83% of the total variance across the 32 models and on a multimodel mean basis explains 72% of the total variance (Fig. 2*A*). The second mode does not show an intermodel consensus in its response to greenhouse warming (further details are discussed in *Influence from SST beyond the Pacific Ocean*). Like in observations, we mainly focus on the variability change of PC1.

The PC1 is related to Niño4 SST variability, in particular to an incipient CP La Niña when the JJA Niño4 index is negative, accompanied by anomalous warming over the Maritime Continent/South China Sea region (Fig. 2*B*). In every model, a statistically significant (95%) correlation is produced between the PC1 and the Niño4 SST index, and the simulated correlation between the PC1 and the Niño4 index aggregated over all models is high and statistically significant (Fig. 2*C*), and this conclusion holds even if CP El Niño samples are excluded. In contrast to the observed, involvement of the tropical Atlantic is weak owing to a weaker tropical Atlantic influence on the Pacific (46, 48). Nevertheless, simulation of WPSH variability and its dynamics is reasonable.

We first compare simulated WPSH variability between the periods 2000 to 2020 and 1979 to 1999. The multimodel ensemble mean shows an increase of 4%, indicating a potential impact from greenhouse warming. However, only a total of 19 out of 32 (59%) models generate an increase (*SI Appendix*, Fig. S5). The intermodel consensus is low and does not exceed 68%, and the multimodel ensemble mean increase in not statistically significant, suggesting that any influence from greenhouse warming is yet to emerge out of internal variability. Despite this, below we show greenhouse warming during the past 42 y should have generated an increase in WPSH variability even though it is yet to emerge out of internal variability.

Downloaded from https://www.pnas.org by CSIRO Library Services on May 31, 2022 from IP address 140.253.235.29.

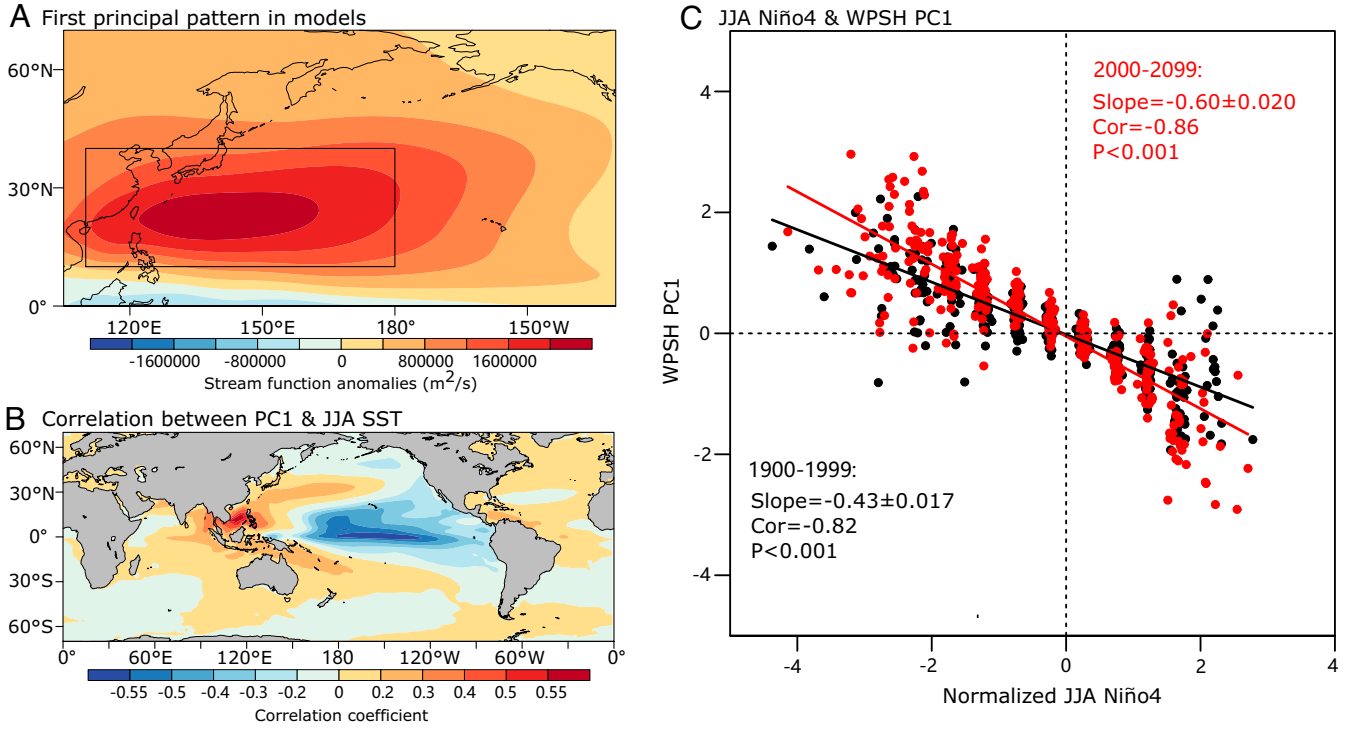

Fig. 2. WPSH variability and mechanism in CMIP6 models. (*A*) Multimodel average of JJA 850-hPa stream function anomaly (square meters per second) pattern obtained by regression onto modeled first PC (PC1) of EOF of JJA 850-hPa stream function anomalies over the northwest Pacific (10°N-40°N, 110°E-180°E) in the period of 1900 to 2099. (*B*) Multimodel average correlations of JJA SST anomalies with PC1. (*C*) Relationship between normalized Niño4 and PC1 aggregated over 32 CMIP6 models for the present-day (1900 to 1999) and future (2000 to 2099) climate, with a linear fit (solid line) and statistical properties shown, including the slope of the linear fit (Slope) and its SE, correlation coefficient (Cor) and *P* value (P). In each model, Niño4 and PC1 are averaged in bins of 0.5 intervals. The models reasonably simulate the observed WPSH variability and its relationship with Niño4 SST.

We compare variability of the PC1 between the 20th- (1900 to 1999) and 21st-century (2000 to 2099) climate. A total of 30 out of 32 models (94%) show an increase in PC1 variability from the 20th century to the future period (Fig. 3*A*). The strong intermodel consensus is supported by a multimodel ensemble mean increase of 16%, statistically significant above the 95% confidence level according to a bootstrap test (see *Statistical Test*). The increase in variability translates to an increased frequency of strong WPSH events, defined as when the PC1 is greater than 1.5 SD. A total of 27 out of the 32 (84%) models produce a higher frequency of strong WPSH events in 2000 to 2099. The multimodel ensemble mean frequency increases by 73%, from 4.5 events per century in the 20th century to 7.8 events per century in the 21st century (Fig. 3*B*). The conclusion of an increased frequency of the strong WPSH is not sensitive to the threshold used (*SI Appendix*, Fig. S6).

The increase in WPSH variability in response to greenhouse warming is further supported by results from CMIP5 models. We analyze 35 available CMIP5 models forced by historical emissions of greenhouse gases before 2005 and a Representative Concentration Pathway 8.5 (RCP8.5) (49) from 2006 to 2099, equivalent to the SSP5–8.5 emission scenario (see *CMIP Models*). An analysis identical to that conducted for CMIP6 models finds that 27 out of 35 CMIP5 models (77%) generate an increase in WPSH PC1 variability, translating into a multimodel ensemble mean increase of 11% in WPSH PC1 variability and 56% in occurrences of strong WPSH events (*SI Appendix*, Fig. S7).

An increased variability of PC1 and generally unchanged variability of PC2 result in an increased variability of WPSH in the future. The total variability of WPSH, defined as stream function anomalies averaged over 15°N-25°N, 120°E-150°E, shows an increase in the future climate supported by 84% of the models (27 out of the 32 models show an increase) (*SI Appendix*, Fig. S8 *A* and *B*). Models that generate a greater increase in WPSH stream function index variability systematically generate a greater increase in the detrended WPSH geopotential height index variability and WPSH zonal wind shear index variability (*SI Appendix*, Fig. S8*C*), suggesting that the long-term increase in the mean geopotential height associated with the rising tropospheric temperatures under global warming is accompanied by the increase in WPSH variability that rides on the long-term trend.

Thus, by comparing simulated 100-y-long WPSH variability between the 20th and 21st centuries we show that greenhouse warming leads to increased WPSH variability. It follows that greenhouse warming over the past 42 y should have contributed to the increase in WPSH variability over the period 1979 to 2020 discussed above.

Higher Sensitivity to CP SST in a Warming Climate

The increase in WPSH variability and in frequency of strong WPSH events underpinned by the strong intermodel consensus is despite the fact that only half of the models (16 out of 32, or 50%) produce an increase in JJA Niño4 SST variability, suggesting that the increase in WPSH variability is not due to a change in JJA Niño4 SST variability (*SI Appendix*, Fig. S9). Instead, the increase in WPSH variability results from an increased WPSH sensitivity to Niño4 SST under global warming.

We calculate the sensitivity by regressing the PC1 onto the Niño4 index separately for the 20th century and the 21st century to obtain the change between the two periods. To facilitate intermodel comparison, changes in WPSH variability and in

Downloaded from https://www.pnas.org by CSIRO Library Services on May 31, 2022 from IP address 140.253.235.29.

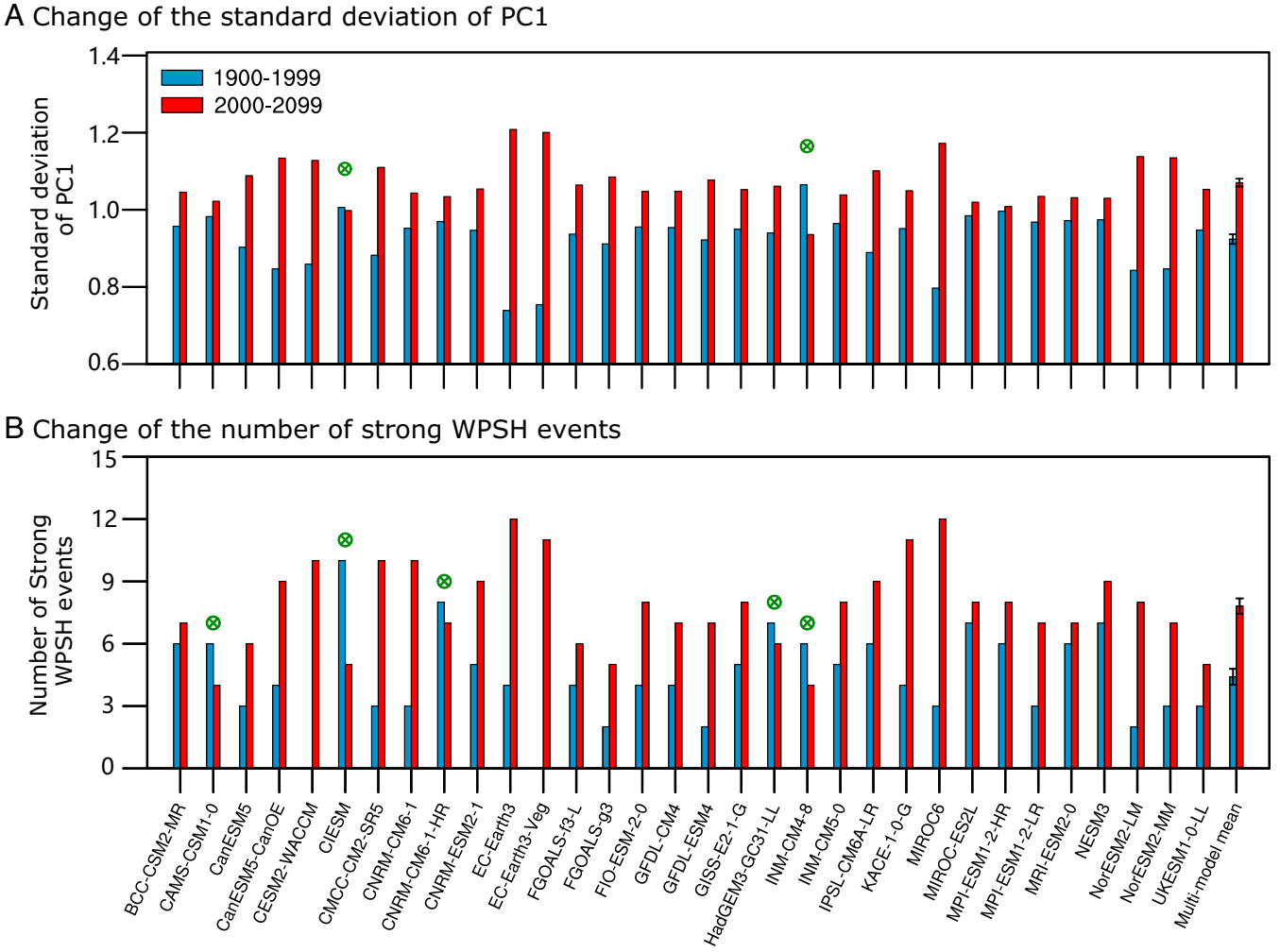

Fig. 3. Projected changes of WPSH variability and strong events. (*A*) A total of 30 out of the 32 CMIP6 models (94%) generate an increase in WPSH PC1 variability from the 20th-century (blue bars) to the 21st-century (red bars) climate. The multimodel mean of the increase is 16%, which is statistically significant above the 95% confidence level (see *Statistical Test*). (*B*) The increase in WPSH PC1 variability translates into a 73% increase in the frequency of strong WPSH events defined as when PC1 > 1.5 SD. The increased frequency is supported by a strong intermodel consensus, with 84% (27 out of the 32) models simulating an increase and is statistically significant (see *Statistical Test*). Models show a decrease are marked by green circles.

the sensitivity are both scaled by the corresponding rise in global mean temperature in each model. In most models, the sensitivity increases, and a greater increase in WPSH sensitivity is systematically associated with a greater increase in WPSH variability (Fig. 4*A*). An overall increased sensitivity of the WPSH to Niño4 is also seen among models (Fig. 2*C*).

Similarly, for each model, we calculate sensitivity of tropical atmosphere convection to Niño4 SST by regressing grid-point outgoing longwave radiation (OLR) anomalies at the top of the atmosphere to the Niño4 index in each period separately to obtain pattern of change in convective sensitivity, scaled by the corresponding global mean temperature rise. The multimodel ensemble mean over the 32 models shows an overall increase in convective sensitivity in the future period. In response to same-sized CP negative SST anomalies, the pattern of depressed convection in the central to eastern Pacific but enhanced convection in the western Pacific and the Maritime Continent, and vice versa, for CP positive SST anomalies is stronger in the 21st-century than in the 20th-century climate (Fig. 4*B*). Consequently, there is a commensurate increase in sensitivity of grid-point 850 hPa stream function anomalies to the Niño4 index, obtained similarly as for the grid-point OLR. The multimodel ensemble mean change in the circulation sensitivity features a stronger anomalous anticyclonic circulation response over the northwestern Pacific to the same Niño4 cooling in the 21st century than in the 20th century (Fig. 4*C*).

That the increased atmosphere convective sensitivity is systematically responsible for enhanced sensitivity of the northwest Pacific stream function is further illustrated in an intermodel relationship between changes in the convective sensitivity pattern and changes in the circulation sensitivity pattern. For each model, we obtain intensity of the convective sensitivity change, and of the circulation sensitivity change, by a pattern regression of an individual-model change pattern onto the ensemble-mean pattern. A greater change in the tropical Pacific convective sensitivity leads to a greater circulation sensitivity (Fig. 4*D*), and therefore a greater increase in WPSH variability.

Several factors are responsible for the increased convective sensitivity. These include a faster warming in the Maritime Continent than in the CP such that atmosphere convection is more likely to move to the Maritime Continent, generating greater convective anomalies (23), and a generally more sensitive atmosphere to the SST anomalies because of the Clausius–Clapeyron relationship, whereby saturation vapor pressure increases exponentially with the increasing temperature (50). As such, response of the tropical humidity and

Downloaded from https://www.pnas.org by CSIRO Library Services on May 31, 2022 from IP address 140.253.235.29.

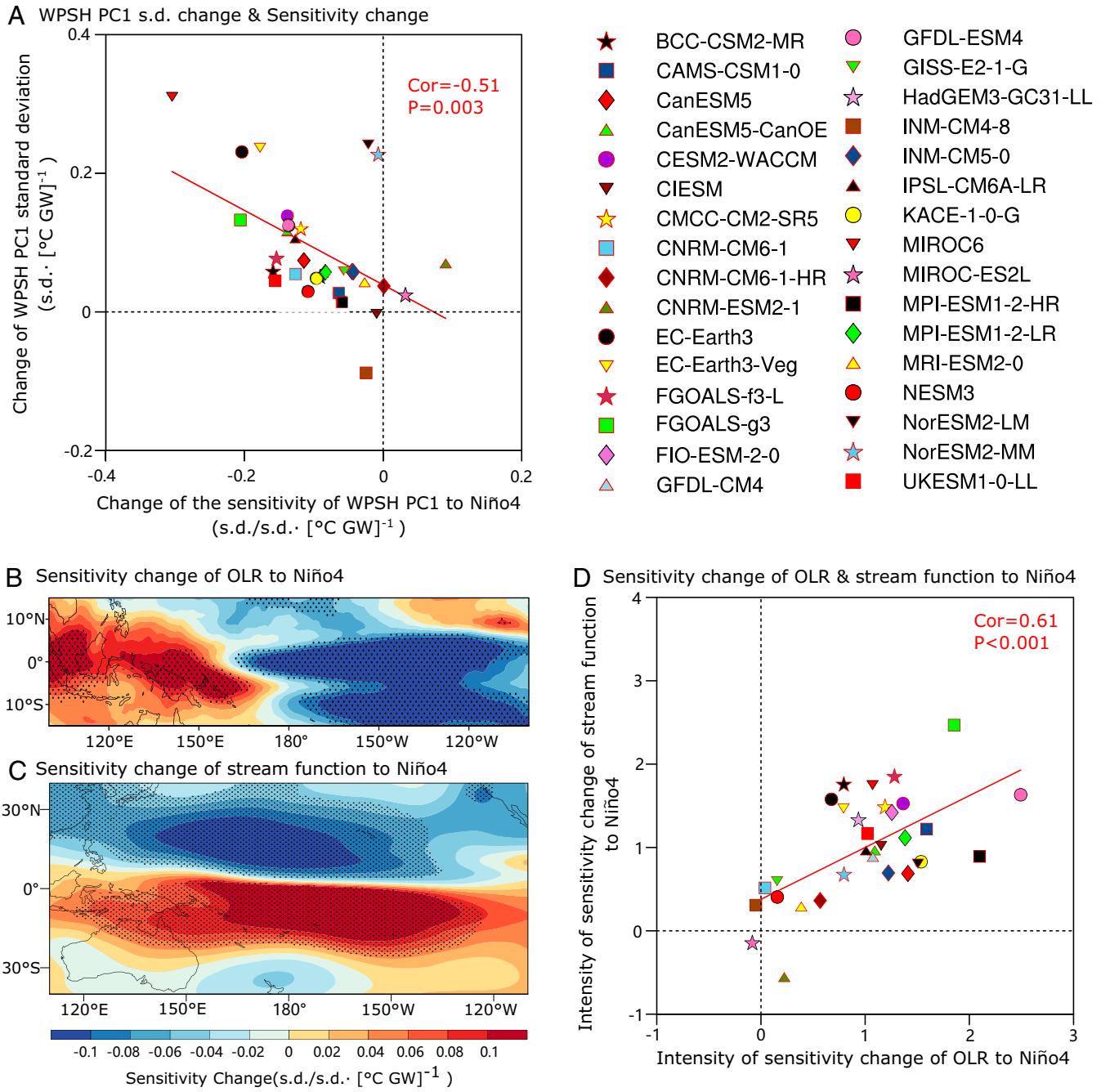

Fig. 4. Mechanisms for projected changes of WPSH. (*A*) Intermodel relationship between projected changes in WPSH PC1 variability and changes in sensitivity of WPSH to JJA Niño4 using 32 CMIP6 models, scaled by global warming rate in each model. A linear fit (red line) and statistical property are shown. The sensitivity is calculated as the regression coefficient of PC1 onto Niño4. JJA Niño4 has been normalized over the whole period first. (*B*) Multimodel average of projected change in sensitivity of JJA OLR to JJA Niño4 scaled by global warming rate in each model. Stippled areas indicate where the multimodel averaged change is statistically significant above the 95% confidence level according to a two-tailed Student's *t* test. (*C*) Same as *B* but for JJA stream function. The OLR and stream function anomalies in each grid have been normalized over the whole period in each model before calculating the sensitivity. (*D*) Intermodel relationship between intensity of the projected change in the OLR sensitivity pattern shown in *B* and in the stream function sensitivity pattern shown in *C*. The intensity is calculated by regressing the sensitivity change pattern scaled by global warming rate in each model onto the multimodel mean sensitivity change pattern in the domain of (10°S-10°N, 100°E-120°W) for OLR and (30°S-30°N, 110°E-120°W) for stream function. A linear fit and statistical properties are shown in red. An increased sensitivity of tropical convection to Niño4 in warming climate leads to an increased response of atmosphere circulation to Niño4 variability and hence strengthened WPSH variability.

associated gross moist instability to SST anomalies is larger in a warmer world of the 21st century than in the 20th century.

Impact from Internal Variability

To examine the possibility that the increase in WPSH variability is due to chances or internal variability, we make use of a set of 40-member simulation experiments with the Community Earth System Model Large Ensemble (CESM-LE) (39) (see *Large Ensemble Experiments*). These experiments are forced similarly to CMIP5 models, starting from 1920, and the only difference among them is a small perturbation in the initial condition resulting in different internal variability (51). We compare the change between the two 90-y periods: 1920 to 2009 and 2010 to 2099.

Downloaded from https://www.pnas.org by CSIRO Library Services on May 31, 2022 from IP address 140.253.235.29.

Without impact from greenhouse warming, there would be a 50 ± 18% chance of generating an increase or decrease in WPSH variability. However, like in CMIP5 or CMIP6 models, the set of experiments produce an increase in WPSH variability in 35 out of 40 (88%) experiments (*SI Appendix*, Fig. S10), with a statistically significant increase in the multiexperiment ensemble mean change. Further, the increase in WPSH variability similarly results from an enhanced sensitivity to Niño4 SST variability (*SI Appendix*, Fig. S11; see *Large Ensemble Experiments*).

We also apply outputs of an 1800-y preindustrial (PI)-control experiment using the CESM. The PI-control simulation, with no greenhouse warming forcing, is used to measure the impact of internal variability on the WPSH. We calculate 1,700 sets of 90-y SD of the WPSH index by constructing 1,700 sets of 90-y continuous time series of WPSH index with different starting year. We then rank the 1,700 values of 90-y SD of the WPSH index from the smallest to the largest (*SI Appendix*, Fig. S12) and identify the 95th percentile value to represent the upper bound of magnitude of WPSH variability associated with internal variability.

The 95th percentile value of the 90-y SD is 2.9×10^6 m^2/s, which is larger than the CESM-LE 40-experiment ensemble mean value (2.7×10^6 m^2/s) of the WPSH index SD during the period 1920 to 2009. Further, only 7 out of the total 40 experiments have an SD larger than 2.9×10^6 m^2/s (*SI Appendix*, Fig. S12). Thus, although greenhouse warming has already been proceeding in 1920 to 2009, its impact on WPSH variability has not emerged out of internal variability.

By contrast, the 40-experiment ensemble mean value of the WPSH index variability during 2010 to 2099 (future period defined in CESM-LE) is 3.2×10^6 m^2/s and is larger than the 95th percentile value of the 90-y SD (2.9×10^6 m^2/s) in the PI-control experiment. In addition, 36 out of the total 40 experiments have a WPSH variability larger than 2.9×10^6 m^2/s, indicating that the increased WPSH variability in the future is not due to internal variability but to greenhouse warming (*SI Appendix*, Fig. S12).

We further compare the magnitude of internal variability in different time length over which the statistics are calculated. The SD of the 1,700 values of 90-y SD of WPSH index is 1.8×10^5 m^2/s, while the SD of the 1,700 values of 40-y SD of WPSH index is 3.0×10^5 m^2/s (*SI Appendix*, Fig. S12*A*), supporting the notion that the impact of internal variability is smaller when the time length used to calculate statistics is longer.

In conclusion, the projected increases in WPSH variability and in frequency of strong WPSH events are despite a lack of intermodel consensus on changes in boreal summer SST variability in the central equatorial Pacific. Instead, the increase in WPSH variability is underpinned by a stronger sensitivity of the atmosphere convection to SST in the central equatorial Pacific under greenhouse warming. The higher convective sensitivity in turn generates a greater circulation response, giving rise to higher WPSH variability. The associated increase in the frequency of strong WPSH events means that climate extremes as seen in 1998 and 2020 are projected to occur more frequently (*SI Appendix*, Fig. S13) with severe impacts on lives of the densely populated East Asian countries.

Materials and Methods

Reanalysis Datasets. Monthly wind, stream function, SST, geopotential height, OLR, and precipitation data are from ERA5 (fifth generation of the European Centre for Medium-Range Weather Forecasts atmospheric reanalyses) datasets (52) for the period of 1979 to 2020 with a horizontal resolution of 0.25° × 0.25°. All anomalies are referenced to the climatology over the whole period and linearly detrended. We also use monthly stream function data from NCEP/NCAR (National Centers for Environmental Prediction/National Center for Atmospheric Research) reanalysis (53) and precipitation data from GPCP (Global Precipitation Climatology Project) Version 2.3 Combined Precipitation Data Set (54) over the same period and get similar results.

Indices of WPSH. Variability of the WPSH is conventionally described by geopotential height over the northwestern Pacific. However, geopotential height under greenhouse warming increases with temperature (44, 45). As such, we use stream function to represent the WPSH and apply EOF (41) analysis to the stream function field over the northwestern Pacific (10°N-40°N, 110°E-180°E). The WPSH index defined as regional average of stream function anomalies over the 15°N-25°N, 120°E-150°E is highly correlated with geopotential height anomalies averaged over the same domain and another zonal wind shear index, defined as the zonal wind anomalies difference between 5°N-15°N, 100°E-130°E, and 20°N-30°N, 110°E-140°E (36, 55, 56), with a correlation coefficient of 0.87 and 0.86, respectively. These three indices show a similar ability in depicting the East Asian summer climate.

The leading mode of the EOF based on ERA5 reanalysis explains 77% of the total variance. PC1, scaled to unity, is highly correlated with the regionally averaged stream function anomalies and eddy geopotential height (Fig. 1*C*) both averaged over the 15°N-25°N, 120°E-150°E. Eddy geopotential height is defined as geopotential height anomalies referenced to zonal mean geopotential height over 0 to 40°N and is constructed to remove the increase associated with global warming (44).

PC1 is highly correlated with JJA Niño4 with a correlation coefficient of −0.73 (Fig. 1*E*), while previous research (8, 36) documented that WPSH index defined based on geopotential height and zonal wind shear is not significantly correlated with the concurrent El Niño–Southern Oscillation (ENSO) index. The stream function index tends to have a higher correlation with CP SST than the other indices. The geopotential height index has a larger variance over the higher latitude than over the lower latitudes, whereas the stream function index has a larger loading over the tropical region and therefore is more linked to the CP SST. The distinct relationship of CP SST with the indices is mainly contributed by the nonstrong event years because the WPSH index based on stream function or geopotential height generally identifies the same strong events (Fig.1*C*). The more fundamental cause of the weak correlation is because PC1 is negatively correlated with Niño4, but PC2 is positively correlated with Niño4 at a correlation coefficient of 0.38 (see also Fig. 1 and *SI Appendix*, Fig. S3*B*), such that the total WPSH variability is weakly correlated with CP SST. This further demonstrates the need for a EOF analysis to separate the two parts of WPSH variability.

CMIP Models. We use monthly outputs from 32 climate models participating in CMIP6 (47) and 35 models participating in CMIP5 (49). These models are forced with historical anthropogenic and natural forcings before 2005 for CMIP5 and prior to 2014 for CMIP6 and future greenhouse gases under the RCP8.5 for CMIP5 and the equivalent updated scenario for CMIP6, the SSP5–8.5. Each model simulation covers a 200-y period of 1900 to 2099. To enable intermodel comparison, all data are regridded to a common resolution of 1° longitude by 1° latitude. Monthly anomalies are constructed from a climatological average over the full period 1900 to 2099 before they are quadratically detrended.

Influence from SST beyond the Pacific Ocean. EOF2 of JJA stream function over the northwestern Pacific is associated with a warm north Indian Ocean and a preceding eastern Pacific El Niño (*SI Appendix*, Fig. S3). An anomalous warming in the Indian Ocean occurs in the ensuing summer after an El Niño event matures. The warming causes an anomalous anticyclone at the low troposphere of the northwest Pacific by triggering warm Kelvin waves emanating into the tropical western Pacific, a process referred to as the Indian Ocean capacitor effect (36, 37). In observations PC2 only contributes to half of the strong WPSH events, i.e., 1995 and 2020 (*SI Appendix*, Fig. S3). EOF3 reflects the influence of local SST on WPSH through atmosphere–ocean feedback (8, 27), which explains 4% of the total variance and is not considered further in our analysis of model outputs.

CMIP models simulate a PC2 pattern similar to that in observations. Changes in variability of PC2 between the 20th century and future period show no

Downloaded from https://www.pnas.org by CSIRO Library Services on May 31, 2022 from IP address 140.253.235.29.

intermodel consensus, with 50% of the models showing an increase and the other 50% showing a decrease. The intensity of the anomalous anticyclone associated with a warm Indian Ocean and a preceding El Niño under global warming is influenced by several processes. Similar to the stronger response of EOF1 to the CP La Niña, the anomalous anticyclone induced by the warm Indian Ocean may be stronger under global warming due to the increased sensitivity of tropospheric temperature to SST anomalies (57). However, rainfall and latent heat anomalies over the Indian Ocean associated with SST anomalies are weaker because of an increase in static stability of the boundary layer in a warmer climate, unfavorable for formation of anomalous anticyclone over the northwest Pacific (58). In addition, a projected smaller SST gradient between the tropical Indian Ocean and the northwest Pacific also weakens the anomalous anticyclone associated with the preceding El Niño (59). Competition of these processes and intermodel differences in ENSO property, such as El Niño decaying pace (60), contribute to the intermodel divergence of the projected change in PC2 variability.

Statistical Test. We use a bootstrap test (61) to examine whether the increased WPSH variance is statistically significant. We randomly resample the 32 WPSH index SD values of the CMIP6 models in the 20th-century climate (1900 to 1999) to form 10,000 realizations of 32-sample mean SD. Each resampling process for a realization is independent and any of the 32 samples can be repeated. The same is carried out for the 21st-century climate (2000 to 2099). The multimodel ensemble mean increase in WPSH variability between the 20th-century and 21st-century climate is statistically significant above the 95% confidence level if the multimodel mean increase in WPSH index SD between the two centuries is greater than the sum of the SDs of the 10,000 interrealizations in the 20th-century and 21st-century climate.

Large Ensemble Experiments. We take 40 members of simulation experiments of the CESM-LE (39) to examine the role of internal variability. These experiments are subject to greenhouse warming that follows the CMIP5 design protocol (49) with historical emissions of greenhouse gases from 1850/1920 to 2005 and RCP8.5 forcing from 2006 to 2100. Ensemble member 1 was carried out from 1850, and the other members were created from perturbations of ensemble member 1 in 1920. The initial conditions are identical (end of 1919), except with an imposed infinitesimally small random perturbation to the atmospheric state at the level of machine round-off error (10^{-14} °C in air temperature) at the beginning of 1920. Therefore, any subsequent difference between model experiment members is due to internal variability (51).

Results from CESM-LE strengthen the conclusions and mechanisms in CMIP models. The multiexperiment mean EOF1 pattern is similar to those in observation and CMIP models (*SI Appendix*, Fig. S10 *A* and *B*). We compare changes between the initial 90 y (1920 to 2009) and last 90 y (2010 to 2099). Among the 40 experiments, 35 (88%) experiments show an increase in WPSH variability in the future. The multiexperiment increase is significant above the 95% confidence level according to the bootstrap test (*SI Appendix*, Fig. S10*C*). The interexperiment difference in the WPSH variability change is due to the internal variability, in which the change in Niño4 variability plays an important role (*SI Appendix*, Fig. S11*A*). Similar to CMIP6, the change in Niño4 variability under greenhouse warming shows no interexperiment consensus (*SI Appendix*, Fig. S11*A*), but an increased sensitivity of WPSH index to Niño4 leads to the increase in WPSH variability (*SI Appendix*, Fig. S11*B*).

Data Availability. All study data are included in the article and/or *SI Appendix*.

ACKNOWLEDGMENTS. This work is supported by the National Natural Science Foundation of China (42141019, 41831175, 91937302, and 42105032), the Strategic Priority Research Program of Chinese Academy of Sciences (XDB40000000 and XDA20060501), The Second Tibetan Plateau Scientific Expedition and Research (STEP) program (2019QZKK0102), and the China Postdoctoral Science Foundation (2018M640168). W.C., G.W., and B.N. are supported by the Center for Southern Hemisphere Oceans Research, a joint research Center for Southern Hemisphere Oceans Research between Qingdao National Laboratory for Marine Science and Technology and the Commonwealth Scientific and Industrial Research Organisation. We acknowledge the World Climate Research Programme's Working Group on Coupled Modelling, which is responsible for CMIP, and we thank the climate modeling groups for producing and making available their model output. For CMIP, the US Department of Energy's Program for Climate Model Diagnosis and Intercomparison provides coordinating support and led development of software infrastructure in partnership with the Global Organization for Earth System Science Portals. We are grateful to the reanalysis groups for making the datasets publicly available.

Author affiliations: [a]State Key Laboratory of Numerical Modeling for Atmospheric Sciences and Geophysical Fluid Dynamics, Institute of Atmospheric Physics, Chinese Academy of Sciences, Beijing 100029, China; [b]Key Laboratory of Physical Oceanography–Institute for Advanced Ocean Studies, Ocean University of China and Qingdao National Laboratory for Marine Science and Technology, Qingdao 266003, China; [c]Center for Southern Hemisphere Oceans Research, CSIRO Oceans and Atmosphere, Hobart, TAS 7004, Australia; [d]Laboratory for Regional Oceanography and Numerical Modeling, Qingdao National Laboratory for Marine Science and Technology, Qingdao 266237, China; and [e]University of Chinese Academy of Sciences, Beijing 100049, China

1. S. Y. Tao, L. X. Liu, A review of recent research on the East Asian summer monsoon in China. *Monsoon Meteorol.* **1987**, 60–92 (1987).
2. Y. Ding, C. L. C. Johnny, The East Asian summer monsoon: An overview. *Meteorol. Atmos. Phys.* **89**, 117–142 (2005).
3. R. Zhang, A. Sumi, M. Kimoto, A diagnostic study of the impact of El Niño on the precipitation in China. *Adv. Atmos. Sci.* **16**, 229–241 (1999).
4. C. P. Chang, Y. Zhang, T. Li, Interannual and interdecadal variations of the East Asian summer monsoon and tropical Pacific SSTs. Part I: Roles of the subtropical ridge. *J. Clim.* **13**, 4310–4325 (2000).
5. T. Zhou *et al.*, Why the Western Pacific subtropical high has extended westward since the late 1970s. *J. Clim.* **22**, 2199–2215 (2009).
6. T. Tomita, T. Yoshikane, T. Yasunari, Biennial and lower-frequency variability observed in the early summer climate in the Western North Pacific. *J. Clim.* **17**, 4254–4266 (2004).
7. E.-J. Lee, J.-G. Jhun, C.-K. Park, Remote connection of the Northeast Asian summer rainfall variation revealed by a newly defined monsoon index. *J. Clim.* **18**, 4381–4393 (2005).
8. B. Wang, B. Xiang, J.-Y. Lee, Subtropical high predictability establishes a promising way for monsoon and tropical storm predictions. *Proc. Natl. Acad. Sci. U.S.A.* **110**, 2718–2722 (2013).
9. Z.-Q. Zhou, S.-P. Xie, R. Zhang, Historic Yangtze flooding of 2020 tied to extreme Indian Ocean conditions. *Proc. Natl. Acad. Sci. U.S.A.* **118**, e2022255118 (2021).
10. Huaxia, China raises flood response to second-highest level. www.xinhuanet.com/english/2020-07/12/c_139207054.htm. *Xinhua News*, 12 July 2020. Accessed 12 February 2021.
11. S. N. Jonkman, Global perspectives on loss of human life caused by floods. *Nat. Hazards* **34**, 151–175 (2005).
12. W. Choi, K.-Y. Kim, Summertime variability of the western North Pacific subtropical high and its synoptic influences on the East Asian weather. *Sci. Rep.* **9**, 7865 (2019).
13. C. He, T. Zhou, Responses of the Western North Pacific subtropical high to global warming under RCP4.5 and RCP8.5 scenarios projected by 33 CMIP5 models: The dominance of Tropical Indian Ocean–Tropical Western Pacific SST Gradient. *J. Clim.* **28**, 365–380 (2015).
14. B. Preethi, M. Mujumdar, A. Prabhu, R. Kripalani, Variability and teleconnections of South and East Asian summer monsoons in present and future projections of CMIP5 climate models. *Asia-Pac. J. Atmospheric Sci.* **53**, 305–325 (2017).
15. A. Cherchi *et al.*, The response of subtropical highs to climate change. *Curr. Clim. Change Rep.* **4**, 371–382 (2018).
16. W. Li, L. Li, M. Ting, Y. Liu, Intensification of Northern Hemisphere subtropical highs in a warming climate. *Nat. Geosci.* **5**, 830–834 (2012).
17. X. Chen, T. Zhou, P. Wu, Z. Guo, M. Wang, Emergent constraints on future projections of the western North Pacific Subtropical High. *Nat. Commun.* **11**, 2802 (2020).
18. R. Lu, B. Dong, Westward extension of North Pacific subtropical high in summer. *J. Meteorol. Soc. Japan. Ser. II* **79**, 1229–1241 (2001).
19. H. Li, F. Xu, Y. Lin, The impact of SST on the zonal variability of the Western Pacific subtropical high in boreal summer. *J. Geophys. Res.: Atmos.* **125**, e2019JD031720 (2020).
20. S. Matsumura, T. Horinouchi, Pacific Ocean decadal forcing of long-term changes in the western Pacific subtropical high. *Sci. Rep.* **6**, 37765 (2016).
21. S. Matsumura, S. Sugimoto, T. Sato, Recent intensification of the Western Pacific subtropical high associated with the East Asian summer monsoon. *J. Clim.* **28**, 2873–2883 (2015).
22. K.-S. Yun, S.-W. Yeh, K.-J. Ha, Distinct impact of tropical SSTs on summer North Pacific high and western North Pacific subtropical high. *J. Geophys. Res. D Atmospheres* **118**, 4107–4116 (2013).
23. W. Cai *et al.*, Increased frequency of extreme La Niña events under greenhouse warming. *Nat. Clim. Chang.* **5**, 132–137 (2015).
24. Z. Chen, Z. Wen, R. Wu, X. Lin, J. Wang, Relative importance of tropical SST anomalies in maintaining the Western North Pacific anomalous anticyclone during El Niño to La Niña transition years. *Clim. Dyn.* **46**, 1027–1041 (2016).
25. T. Li *et al.*, Theories on formation of an anomalous anticyclone in western North Pacific during El Niño: A review. *J. Meteorol. Res.* **31**, 987–1006 (2017).
26. M. F. Stuecker, F.-F. Jin, A. Timmermann, S. McGregor, Combination mode dynamics of the anomalous Northwest Pacific anticyclone. *J. Clim.* **28**, 1093–1111 (2015).
27. B. Xiang, B. Wang, W. Yu, S. Xu, How can anomalous western North Pacific Subtropical High intensify in late summer? *Geophys. Res. Lett.* **40**, 2349–2354 (2013).
28. L. Fan, S.-I. Shin, Q. Liu, Z. Liu, Relative importance of tropical SST anomalies in forcing East Asian summer monsoon circulation. *Geophys. Res. Lett.* **40**, 2471–2477 (2013).
29. N.-C. Lau, M. Nath, ENSO modulation of the interannual and intraseasonal variability of the East Asian Monsoon–A model study. *J. Clim.* **19**, 4508–4530 (2006).
30. P.-H. Chung, C.-H. Sui, T. Li, Interannual relationships between the tropical sea surface temperature and summertime subtropical anticyclone over the western North Pacific. *J. Geophys. Res. D Atmospheres* **116**, D13111 (2011).

Downloaded from https://www.pnas.org by CSIRO Library Services on May 31, 2022 from IP address 140.253.235.29.

31. C.-H. Sui, P.-H. Chung, T. Li, Interannual and interdecadal variability of the summertime western North Pacific subtropical high. *Geophys. Res. Lett.* **34**, L11701 (2007).
32. B. Wu, T. Zhou, Oceanic origin of the interannual and interdecadal variability of the summertime western Pacific subtropical high. *Geophys. Res. Lett.* **35**, L13701 (2008).
33. Y.-G. Ham, J.-S. Kug, J.-Y. Park, F.-F. Jin, Sea surface temperature in the north tropical Atlantic as a trigger for El Niño/Southern Oscillation events. *Nat. Geosci.* **6**, 112–116 (2013).
34. C.-C. Hong, M.-Y. Lee, H.-H. Hsu, N.-H. Lin, B.-J. Tsuang, Tropical SST forcing on the anomalous WNP subtropical high during July–August 2010 and the record-high SST in the tropical Atlantic. *Clim. Dyn.* **45**, 633–650 (2015).
35. J. Zuo, W. Li, C. Sun, H.-C. Ren, Remote forcing of the northern tropical Atlantic SST anomalies on the western North Pacific anomalous anticyclone. *Clim. Dyn.* **52**, 2837–2853 (2019).
36. S.-P. Xie *et al.*, Indian ocean capacitor effect on Indo–Western pacific climate during the summer following El Niño. *J. Clim.* **22**, 730–747 (2009).
37. J. Yang, Q. Liu, S.-P. Xie, Z. Liu, L. Wu, Impact of the Indian Ocean SST basin mode on the Asian summer monsoon. *Geophys. Res. Lett.* **34**, L02708 (2007).
38. K. Hu, G. Huang, S.-P. Xie, Assessing the internal variability in multi-decadal trends of summer surface air temperature over East Asia with a large ensemble of GCM simulations. *Clim. Dyn.* **52**, 6229–6242 (2019).
39. J. E. Kay *et al.*, The Community Earth System Model (CESM) large ensemble project: A community resource for studying climate change in the presence of internal climate variability. *Bull. Am. Meteorol. Soc.* **96**, 1333–1349 (2015).
40. J. M. Wallace, C. Deser, B. V. Smoliak, A. S. Phillips, "Attribution of climate change in the presence of internal variability" in *Climate Change: Multidecadal and Beyond*, C.-P. Chang, M. Ghil, M. Latif, J. M. Wallace, Eds. (*World Scientific Series on Asia-Pacific Weather and Climate*, World Scientific, 2013), **vol. 6**, pp. 1–29.
41. E. N. Lorenz, "Empirical orthogonal functions and statistical weather prediction" (Statistical Forecast Project Report 1, Department of Meteorology, Massachusetts Institute of Technology, 1956).
42. B. Jia, J. Peng, S. Hu, G. Feng, Novel dynamical indices for the variations of the western Pacific subtropical high based on three-pattern decomposition of global atmospheric circulation in a warming climate. *Clim. Dyn.* **56**, 3473–3487 (2021).
43. Y. Huang, H. Wang, K. Fan, Y. Gao, The western Pacific subtropical high after the 1970s: Westward or eastward shift? *Clim. Dyn.* **44**, 2035–2047 (2015).
44. C. He *et al.*, Enhanced or weakened Western North Pacific subtropical high under global warming? *Sci. Rep.* **5**, 16771 (2015).
45. L. Wu, C. Wang, Has the Western Pacific subtropical high extended westward since the late 1970s? *J. Clim.* **28**, 5406–5413 (2015).
46. W. Cai *et al.*, Pantropical climate interactions. *Science* **363**, eaav4236 (2019).
47. V. Eyring *et al.*, Overview of the Coupled Model Intercomparison Project Phase 6 (CMIP6) experimental design and organization. *Geosci. Model Dev.* **9**, 1937–1958 (2016).
48. F. Jia *et al.*, Weakening Atlantic Niño-Pacific connection under greenhouse warming. *Sci. Adv.* **5**, eaax4111 (2019).
49. K. E. Taylor, R. J. Stouffer, G. A. Meehl, An Overview of CMIP5 and the experiment design. *Bull. Am. Meteorol. Soc.* **93**, 485–498 (2012).
50. K. Hu, G. Huang, P. Huang, Y. Kosaka, S.-P. Xie, Intensification of El Niño-induced atmospheric anomalies under greenhouse warming. *Nat. Geosci.* **14**, 377–382 (2021).
51. W. Cai *et al.*, Butterfly effect and a self-modulating El Niño response to global warming. *Nature* **585**, 68–73 (2020).
52. H. Hersbach, *et al.*, "ERA5 monthly averaged data on pressure levels from 1979 to present." Copernicus Climate Change Service (C3S) Climate Data Store (CDS). https://cds.climate.copernicus.eu/cdsapp#!/dataset/reanalysis-era5-pressure-levels-monthly-means?tab=overview. Accessed 3 January 2021.
53. E. Kalnay *et al.*, The NCEP/NCAR 40-year reanalysis project. *Bull. Am. Meteorol. Soc.* **77**, 437–472 (1996).
54. R. F. Adler *et al.*, The Version-2 Global Precipitation Climatology Project (GPCP) monthly precipitation analysis (1979–present). *J. Hydrometeorol.* **4**, 1147–1167 (2003).
55. B. Wang, Z. Fan, Choice of South Asian summer monsoon indices. *Bull. Am. Meteorol. Soc.* **80**, 629–638 (1999).
56. G. Huang, K. Hu, S.-P. Xie, Strengthening of tropical Indian Ocean teleconnection to the Northwest Pacific since the mid-1970s: An atmospheric GCM study. *J. Clim.* **23**, 5294–5304 (2010).
57. K. Hu *et al.*, Interdecadal variations in ENSO influences on Northwest Pacific–East Asian early summertime climate simulated in CMIP5 models. *J. Clim.* **27**, 5982–5998 (2014).
58. C. He, T. Zhou, T. Li, Weakened anomalous Western North Pacific anticyclone during an El Niño–decaying summer under a warmer climate: Dominant role of the weakened impact of the tropical Indian Ocean on the atmosphere. *J. Clim.* **32**, 213–230 (2019).
59. W. Jiang, G. Huang, P. Huang, K. Hu, Weakening of Northwest Pacific anticyclone anomalies during post–El Niño summers under global warming. *J. Clim.* **31**, 3539–3555 (2018).
60. M. Wu, T. Zhou, X. Chen, B. Wu, Intermodel uncertainty in the projection of the anomalous Western North Pacific anticyclone associated with El Niño under global warming. *Geophys. Res. Lett.* **47**, e2019GL086139 (2020).
61. P. C. Austin, J. V. Tu, Bootstrap methods for developing predictive models. *Am. Stat.* **58**, 131–137 (2004).

Downloaded from https://www.pnas.org by CSIRO Library Services on May 31, 2022 from IP address 140.253.235.29.